Quadrupole moments in chiral material $DyFe_3(BO_3)_4$ observed by resonant x-ray diffraction

Hiroshi Nakajima,[1,2] Tomoyasu Usui,[1] Yves Joly,[3,4] Motohiro Suzuki,[5] Yusuke Wakabayashi,[1]
Tsuyoshi Kimura,[1] and Yoshikazu Tanaka[6,*]

[1]*Division of Materials Physics, Graduate School of Engineering Science, Osaka University, Toyonaka, Osaka 560-8531, Japan*
[2]*Department of Materials Science, Graduate School of Engineering, Osaka Prefecture University, Sakai, Osaka 599-8531, Japan*
[3]*Université Grenoble Alpes, Institut NEEL, F-38042 Grenoble, France*
[4]*CNRS, Institut NEEL, F-38042 Grenoble, France*
[5]*Japan Synchrotron Radiation Research Institute (JASRI), Sayo, Hyogo 679-5198, Japan*
[6]*RIKEN SPring-8 Center, Sayo, Hyogo 679-5148, Japan*

(Received 28 September 2015; revised manuscript received 29 March 2016; published 18 April 2016)

By means of circularly polarized x rays at the Dy L_3 and Fe K absorption edges, the chiral structure of the electric quadrupole was investigated for a single crystal of $DyFe_3(BO_3)_4$, in which both Dy and Fe ions exhibit a spiral arrangement. The integrated intensity of the resonant x-ray diffraction of space-group forbidden reflections 004 and 005 is interpreted within the electric dipole transitions from Dy $2p_{\frac{3}{2}}$ to $5d$ and Fe $1s$ to $4p$, respectively. We have confirmed that the handedness of the crystal observed at Dy L_3 and Fe K edges is consistent with that observed at Dy M_5 edge reported in a previous study. The electric quadrupole moments of Dy $5d$ and Fe $4p$ are derived by analyzing the azimuth scans of the diffracted intensity. The temperature profiles of the integrated intensity of 004 at the Dy L_3 and the Fe K edges are similar to those of Dy-O and Fe-O bond lengths, while the temperature dependence at the Dy M_5 edge does not match the bond-length behavior. The results indicate that the helix chiral orientations of quadrupole moments due to Dy $5d$ and Fe $4p$ electrons are more strongly coupled to the ligands states than Dy $4f$ electrons.

DOI: 10.1103/PhysRevB.93.144116

I. INTRODUCTION

Chirality is one of the most important concepts over a wide range of science, including particle physics, cosmology, biology, pharmacy, condensed matter physics, and industry, etc. [1,2]. The key issue of chirality, or handedness, is the breaking of symmetry that plays a crucial role in a variety of fields. In condensed matter physics, the breaking of symmetry often gives an excellent arena to manipulate the physical properties. One prominent example is found in the magnetoelectric multiferroic materials, where the ferroelectricity appears as a result of a phase transition which induces a magnetic order with broken inversion symmetry [3,4]. Many multiferroics have a cycloidal or a screw spin structure, the handedness of which determines the sign of the spontaneous electric polarization. In such a system, the multipole moments demonstrate the sign of handedness together with the atomic and spin structure.

In this paper, we use the term "multipole order" to express the order of the electron density rather than the term "orbital order." There have been many studies [5,6] where the "orbital order" of the d-electron states in transition-metal compounds were observed and discussed. In principle, the orbital order observed in the d-electron states of transition-metal compounds is another expression of the multipole moment order. Thus, both expressions ("multipole order" and "orbital order") describe the order of the electron density around the ion. This terminological difference depends on how the degeneracy of the electronic state is lifted. Energy balance between the crystal field and the spin-orbit coupling plays a role in lifting the degeneracy. In the $3d$ transition-metal compounds, the crystal field effectively exerts the orbital splitting, which drives the orbital order. On the other hand, in the $4f$ rare-earth compounds, the spin-orbit coupling is so strong that the electronic state is described by the total angular momentum J. The quadrupole order, or the higher multipole order including the spin state, appears in the ground state of the J multiplets as a result of the crystal field splitting and other interactions such as Ruderman-Kittel-Kasuya-Yosida (RKKY) interaction.

The electron density $\rho(\mathbf{r})$ around the ion can be expanded in terms of the electric multipoles $\rho(\mathbf{r}) = \sum_{l,m} \rho_{lm}(r) Y_l^m(\hat{\mathbf{r}})$ with $-l \leqslant m \leqslant l$. Thus, we get $\rho_{lm}(r) = \int \rho(\mathbf{r}) Y_l^{m*}(\hat{\mathbf{r}}) d\hat{\mathbf{r}}$. Here, $\hat{\mathbf{r}}$ is a radial unit vector. The electric multipoles are directly related to the familiar Cartesian representation, for example, the dipole moment $\mu_i = \int \rho(\mathbf{r}) r_i d\mathbf{r}$, and the quadrupole moments $q_{ij} = \int \rho(\mathbf{r})(3r_i r_j - \delta_{ij} r^2) d\mathbf{r}$ with $r_{i,j} = x,y,z$. Here, $\mu_x = \frac{1}{2}\int \{\rho_{1+1}(r) + \rho_{1-1}(r)\} dr$, $\mu_y = -\frac{i}{2}\int \{\rho_{1+1}(r) - \rho_{1-1}(r)\} dr$, and $\mu_z = \int \rho_{10}(r) dr$. The multipole moments, generally written $\langle T_Q^K \rangle$, are thus a way to give an expected value of the spherical tensor T_Q^K representing the electron density. The spherical tensor is related to the spherical function as $T_Q^K = Y_l^m(\hat{r})$, with $m = Q$ and $l = K$. Here, K represents the rank of tensor, and Q $(-K \leqslant Q \leqslant K)$ its projection. The corresponding spherical harmonics give their angular dependence. For example, one gets for $T_{\pm 1}^2$ and $T_{\pm 2}^2$, respectively, $\sin\vartheta \cos\vartheta e^{\pm i\varphi}$ and $\frac{1}{2}\sin^2\vartheta e^{\pm 2i\varphi}$, where ϑ and φ are the angles in the polar coordinate of the ion concerned. This representation is quite useful in the symmetry operation as we discuss in Sec. VI A. For the spherical electron density, only the $K = 0$ component is not zero. The atomic p or d state as well as the f state can be expanded in terms of the multipole moments. For example, for the atomic wave function $p_z = r\cos\vartheta$, only the monopole (or charge) $(K,Q) = (0,0)$ and quadrupole $(K,Q) = (2,0)$ moments are nonzero within $K \leqslant 2$.

*ytanaka@riken.jp

In principle, the electric multipole $\langle T_Q^K \rangle$ is visible with an x-ray beam because the electron has the large cross section for the x-ray beam. In reality, however, observing a motif of the multipoles in a crystal using x-ray diffraction is not easy. In the conventional x-ray diffraction, which is used to observe the crystal structure, the diffraction profile is mainly derived from the core electrons of the consisting elements in the matter, where the contribution of the valence electrons is negligible. Whereas, if a system has, say, an antiferroic type of the multipole order, where the symmetry of valence electrons breaks the crystal symmetry, the order can be observed with a high-intensity x-ray beam from a synchrotron radiation source. For example, it has been found that the antiferroic quadrupole order in CeB_6 at low temperatures shows tiny superlattice reflections $(\frac{h}{2}, \frac{k}{2}, \frac{l}{2})$, where h, k, and l are odd numbers [7,8].

Since the discovery of linear dichroism [9] and forbidden reflections [10] at an absorption edge, resonant x-ray diffraction (RXD) has been developed to investigate a variety of ordered states, such as magnetic, charge, or orbital orders. The atomic picture of the resonance is well known: an incoming photon promotes a core electron to empty states, and it returns to the same core hole, emitting a second photon of the same energy as the incoming one. The scattering length at an absorption edge, which is sensitive to the polarization in the primary and secondary x rays, carries site-specific information on unoccupied valence states on and around the resonant ion. This sensitivity provides another useful aspect of RXD as described below.

Circular dichroism in RXD has been found for low quartz [11,12], which has an enantiomorphic space-group pair $P3_121$ (right-handed screw) and $P3_221$ (left-handed screw). In crystals having the space-group pair $P3_121$ and $P3_221$, reflections $00l$ ($l \neq 3n$, $n =$ integer) are forbidden in nonresonant x-ray diffraction, but allowed in RXD for certain x-ray energies because of the sensitivity of the atomic scattering length to the x-ray polarization. By carefully examining the space-group forbidden reflections observed with circularly polarized x rays, one can identify the absolute sign of the crystallographic helix chirality [13,14]. For the ferromagnetic or the ferroelectric states, we hardly know the state of the valence electrons by x-ray diffraction because the symmetry of the magnetic order or the charge order is the same as the crystal symmetry. However, for the system having the screw axis or the glide plane, we can scrutinize the ordering state of the multipole moment, observing the space-group forbidden reflections [15], even though the symmetry is the same as the crystal symmetry.

Recently, we have successfully shown that RXD using circularly polarized x rays not only identifies the absolute sign of the crystallographic helix chirality, but also provides direct information on the multipole moments accompanying the crystallographic helix chirality [16]. We have determined two components among five of the $4f$ quadrupole moments of Dy in $DyFe_3(BO_3)_4$ where the motif of the $4f$ quadrupole moment coincides with the crystallographic helix chirality. In the experiment, we have observed forbidden reflection 001 with circularly polarized soft x-ray beam at Dy M_5 absorption edge, where the x rays enhance the resonance from the $3d_{\frac{5}{2}}$ state to the vacant $4f$ state. Accordingly, the signal observed in the diffraction gives the information of the $4f$ quadrupole moment of Dy ions.

In this study, we demonstrate that circularly polarized hard x-ray beam at two absorption edges Dy L_3 and Fe K is also useful to determine the absolute sign of crystal chirality in $DyFe_3(BO_3)_4$, quite like the soft x-ray beam at Dy M_5 absorption edge. The resonance from Dy $2p_{\frac{3}{2}}$ to $5d$ at Dy L_3 absorption edge, and that from Fe $1s$ to $4p$ at Fe K absorption edge, give the information of Dy $5d$ quadrupole moment and the Fe $4p$ quadrupole moment, respectively. We discuss the possibility of the birefringence phenomenon and the higher-order transition like $E1E2$ for the observed data. We also discuss the chirality in terms of the electric Dy $5d$ quadrupole moment and the Fe $4p$ quadrupole moment together with the deformation of the crystal structure as a function of temperature.

We give a general background of resonant x-ray diffraction in Sec. II. We describe the crystal structure of $DyFe_3(BO_3)_4$ as well as the physical properties in Sec. III and the experimental geometry in Sec IV. In Sec. V, we show the experimental results of the resonant diffraction both at Dy L_3 and Fe K absorption edges: x-ray absorption spectra, azimuth angle scans, and the temperature dependence of the integrated intensity of forbidden reflection 004. In Sec. VI, we analyze the azimuth scan data and derive the Dy $5d$ quadrupole moment and the Fe $4p$ quadrupole moment with theoretical interpretations. In addition, we discuss the temperature dependence in terms of the deformation of DyO_6 trigonal prism and FeO_6 octahedron.

II. RESONANT X-RAY DIFFRACTION

The determination of the absolute structure of enantiomers, which are exact mirror images of each other, is not easy because they have the same chemical formula and atom to atom arrangements, and hence it has been considered as an important challenge of crystallography. Among many methods applied for the determination so far, x-ray diffraction with dispersion corrections has played an important role for a long time.

The scattering length of x rays for an atom can be written as

$$f = f_0 + f' + if'', \tag{1}$$

where f_0 is the energy-independent x-ray scattering length and corresponds to the Fourier transform of the electron density around the atom, f' and f'' are the real and the imaginary parts, respectively, of the dispersion correction. Note that the sign of f'', which is positive in conventional x-ray diffraction, is negative in our convention with the phase factor $e^{i(\mathbf{K}\cdot\mathbf{r}-\omega t)}$ with the momentum transfer K from the x rays to the crystal. Since the absolute configuration of the enantiomorphic compounds was determined for tartaric acid [17] using the dispersion correction, this method has developed significantly with the advent of the synchrotron radiation source. It is now known as multiwavelength anomalous diffraction (MAD) [18,19], and has developed extensively to study the absolute configurations of biochemical compounds. The method requires measurements of the diffraction pattern at several energies around the K or L absorption edges of the resonantly scattering elements.

It is well established that one can observe *space-group forbidden* reflections at the resonant energy in the vicinity of the absorption edge, where the scattering length is sensitive to the polarization of the primary and secondary x rays.

Some *forbidden* Bragg reflections become *allowed*, when the equivalency of the local atomic configuration around the resonant scatterer in a unit cell is broken by the screw axis, the glide plane, or the magnetic structure. Pioneering works have been done for the crystallographic study by Templeton *et al.* [10] and for the magnetic structural study by Gibbs *et al.* [20]. We use the circularly polarized x rays in the resonant x-ray diffraction to identify the handedness of the chiral structure. This method requires measurements of a single forbidden reflection in contrast to MAD.

The dispersion correction terms in the vicinity of the absorption edge are written as

$$f' + if'' = m \sum_{n,g} \left(\frac{\Delta}{\hbar} \right)^2 \frac{\langle g|\hat{o}_s^*|n\rangle \langle n|\hat{o}_i|g\rangle}{\hbar\omega - \Delta + i\Gamma/2}, \qquad (2)$$

where g and n label the ground and intermediate states, respectively. The difference energy $\Delta = \mathcal{E}_n - \mathcal{E}_g$, where $\mathcal{E}_g$ and $\mathcal{E}_n$ are their corresponding energies, and $|g\rangle$ and $|n\rangle$ are their wave functions. The electron mass is denoted by m, $\hbar\omega$ is the photon energy, Γ is a phenomenological broadening depending on the excited electron kinetic energy and the core-hole width, and i and s label the incoming and scattered waves. The transition operator, dominated by its electric part and taken to second order, is given by

$$\hat{o} = (\boldsymbol{\epsilon} \cdot \mathbf{r}) \left\{ 1 + \frac{i}{2} (\mathbf{k} \cdot \mathbf{r}) \right\}. \qquad (3)$$

The first term in the equation gives the electric dipole or $E1$ transition and the second one gives the electric quadrupole or $E2$ transition. The compound $DyFe_3(BO_3)_4$ belongs to one of the enantiomorphic space-group pair $P3_121$ and $P3_221$ in the low-temperature phase, where the inversion symmetry is broken, hence, the $E1E2$ term in Eq. (2) is allowed for the forbidden reflections. However, the contribution is possibly negligible as is discussed later.

III. STRUCTURE OF $DyFe_3(BO_3)_4$

The compound $DyFe_3(BO_3)_4$ consists of DyO_6 trigonal prisms with a Dy^{3+} ion in the center, FeO_6 octahedra with a Fe^{3+} ion in the center, and BO_3 triangles with a B^{3+} ion in the center [21]. It belongs to trigonal space group $R32$ (No. 155) at room temperature. The structure has an alternative stacking of BO_3 network planes and Dy plus Fe planes along the c axis. Space group $R32$ belongs to one of the 65 enantiomorphic space groups, and includes the right-handed screws 3_1 or left-handed screws 3_2 inside so that the crystal can have two choices for the atomic configuration. Indeed, the chain of the FeO_6 octahedra can form, in two ways, a right-handed or a left-handed screw along the c axis in $R32$. These two atomic configurations, which are mirror images of each other, coexist in a single crystal with large chiral domains [16].

This compound has a first-order structural phase transition at $T_S \approx 285$ K [22,23], where the right- and left-handed structures in the space group $R32$ transform into the space groups $P3_121$ (No. 152) and $P3_221$ (No. 154), respectively, on decreasing temperature. In these enantiomorphic space-group pair $P3_121$ and $P3_221$, the stacking chain of the Dy^{3+} ions forms in a right-handed or a left-handed screw along the c axis, respectively. Figure 1 displays the atomic structure of the *left-handed* $DyFe_3(BO_3)_4$ in space group $P3_221$. Note that the handedness of the chain of Fe^{3+} ions in the high-temperature $R32$ phase ($T > T_S$) is transferred to that of the screw chain of the Dy^{3+} ions in the low-temperature phase ($T < T_S$). In the low temperatures, this compound has an additional phase transition at $T_N = 38$ K where both of Fe and Dy magnetic moments show an antiferromagnetic (AF) order [22]. In the AF ordered phase, $DyFe_3(BO_3)_4$ exhibits a magnetoelectric effect accompanied by a spin flop [24].

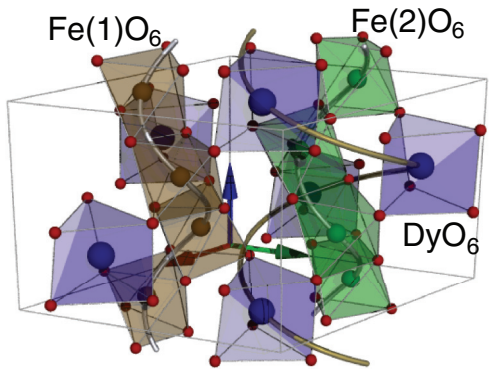

FIG. 1. A view of the atomic configuration of the *left-handed* $DyFe_3(BO_3)_4$ in space group $P3_221$ (No. 154). The FeO_6 octahedra and the DyO_6 trigonal prisms are colored by brown and blue, respectively. The Fe(1) ions are at the $3a$ site, and the Fe(2) are at the $6c$ site. The unit cell is shown by gray lines. Yellow and gray helices represent spiral arrangements of Dy and Fe ions, respectively.

IV. EXPERIMENT

The experiment was carried out at the beam line 29XUL at SPring-8 in Harima, Japan. A subsidiary experiment was carried out at the beam line 3A at the Photon Factory in Tsukuba, Japan. A platelike single crystal of $DyFe_3(BO_3)_4$ was mounted on a copper holder in a liquid He flow-type cryostat on a four-circle diffractometer. The handedness of this crystal has been found to be *left-handed*, space group $P3_221$ (No. 154) in the previous experiment [16]. The sample size was about 2 mm × 2 mm × 0.5 mm. The size of the incident beam was 0.5 mm × 0.5 mm. A scintillation detector was used to observe the diffracted beam. The intensity of the incident beam was monitored by an ionization chamber. The incident energy was tuned by a Si (111) double-crystal monochromator followed by a pair of Si mirrors coated by rhodium in order to cut the higher harmonic x rays at the beam line 29XUL. The helicity of the circularly polarized x-ray beam was manipulated by a diamond phase retarder of 0.6 mm in thickness. We employed the $2\bar{2}0$ reflection of the diamond with its surface being parallel to (111). In the experiment at PF, we used only a $\boldsymbol{\sigma}$ linearly polarized x-ray beam. We measured the intensity of space-group forbidden reflections 004 and 005 at two absorption edges Dy L_3 at $E = 7.796$ keV and Fe K at $E = 7.13$ keV in a temperature range from $T = 30$ to 305 K.

Our diffraction geometry is illustrated in Fig. 2. The azimuth angle Ψ is a rotation of the sample about the scattering vector $\mathbf{K} = \mathbf{k}_i - \mathbf{k}_f$. The vectors $\mathbf{k}_i$ and $\mathbf{k}_f$ are the

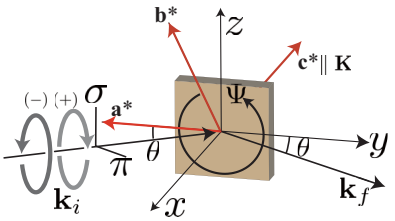

FIG. 2. A schematic view of the diffraction geometry with a right-handed coordinates x, y, and z. The scattering vector $\mathbf{K} = \mathbf{k}_i - \mathbf{k}_f$ is antiparallel to the x axis. The marks (+) and (−) denote the positive and negative helicities of the incident beam, respectively. Here, $\mathbf{k}_i$ and $\mathbf{k}_f$ are the propagation vectors of the incident and diffracted x rays, respectively, and θ denotes the Bragg angle. The $\boldsymbol{\sigma}$ and $\boldsymbol{\pi}$ components are the unit vectors which represent the polarization of the incident beam. Here, the $\boldsymbol{\sigma}$ component is perpendicular to the plane of scattering $\boldsymbol{\sigma} = (0,0,1)$, and the $\boldsymbol{\pi}$ component is parallel to the plane of scattering $\boldsymbol{\pi} = (\cos\theta,\ \sin\theta, 0)$. For the diffracted beam, $\boldsymbol{\sigma}' = \boldsymbol{\sigma}$ and $\boldsymbol{\pi}' = (\cos\theta,\ -\sin\theta, 0)$.

propagation vectors for the incident beam and the diffracted beam, respectively. We define the origin of the azimuth angle $\Psi = 0$ with respect to the direction of the reciprocal lattice vector $\mathbf{a}^*$ when it is parallel to the $-y$ axis, or $\mathbf{a}^* \| -(\mathbf{k}_i + \mathbf{k}_f)$, and the positive direction of Ψ to be the counterclockwise rotation as viewed looking up along the scattering vector $\mathbf{K}$. The polarization of the incident x-ray beam is defined by the unit vectors $\boldsymbol{\sigma}$ and $\boldsymbol{\pi}$.

The average polarization state is expressed with the Stokes parameters P_1, P_2, and P_3 where $P_3 = +1$ and $P_3 = -1$ correspond to the linear polarization parallel to the unit vectors $\boldsymbol{\sigma}$ and $\boldsymbol{\pi}$, respectively, $P_2 = +1$ and $P_2 = -1$ correspond to the circular polarization, represented by $\frac{1}{\sqrt{2}}(\boldsymbol{\sigma} + i\boldsymbol{\pi})$ and $-\frac{1}{\sqrt{2}}(\boldsymbol{\sigma} - i\boldsymbol{\pi})$, respectively, $P_1 = +1$ and $P_1 = -1$ correspond to the linear polarization along the diagonal directions between $\boldsymbol{\sigma}$ and $\boldsymbol{\pi}$, represented by $\frac{1}{\sqrt{2}}(\boldsymbol{\sigma} + \boldsymbol{\pi})$ and $\frac{1}{\sqrt{2}}(\boldsymbol{\sigma} - \boldsymbol{\pi})$, respectively. For the circularly polarized $P_2 = +1$ (-1) state, the $\boldsymbol{\pi}$ $(\boldsymbol{\sigma})$ component lags the $\boldsymbol{\sigma}$ $(\boldsymbol{\pi})$ by 90° according to the phase factor $\exp i(\mathbf{k}\cdot\mathbf{r} - \omega t)$. Here, unit vectors $\boldsymbol{\sigma}$, $\boldsymbol{\pi}$, and $\hat{\mathbf{k}}_i = \mathbf{k}_i/|\mathbf{k}_i|$ satisfy the right-handed rule $\boldsymbol{\sigma} \times \boldsymbol{\pi} = \hat{\mathbf{k}}_i$. The polarization of the beam from the synchrotron radiation source is usually well defined and the relation $P_1^2 + P_2^2 + P_3^2 \cong 1$ holds well.

Resonant x-ray diffraction of space-group forbidden reflections depends on the geometry of the scattering system as well as the energy of the x-ray beam. This is because it depends on the polarization state of the x-ray beam as described by Eq. (3), and the unit-cell structure factor is described by a tensor of the atomic multipoles. Hence, the azimuth angle Ψ scan gives important information not only about the symmetry of the local structure of the resonant ions, but also about the components of the atomic multipoles.

V. RESULTS

A. X-ray absorption spectra

The x-ray absorption spectrum (XAS) and the energy dependence of the space-group allowed reflection 003 in the vicinity of Dy L_3 and Fe K absorption edges are shown

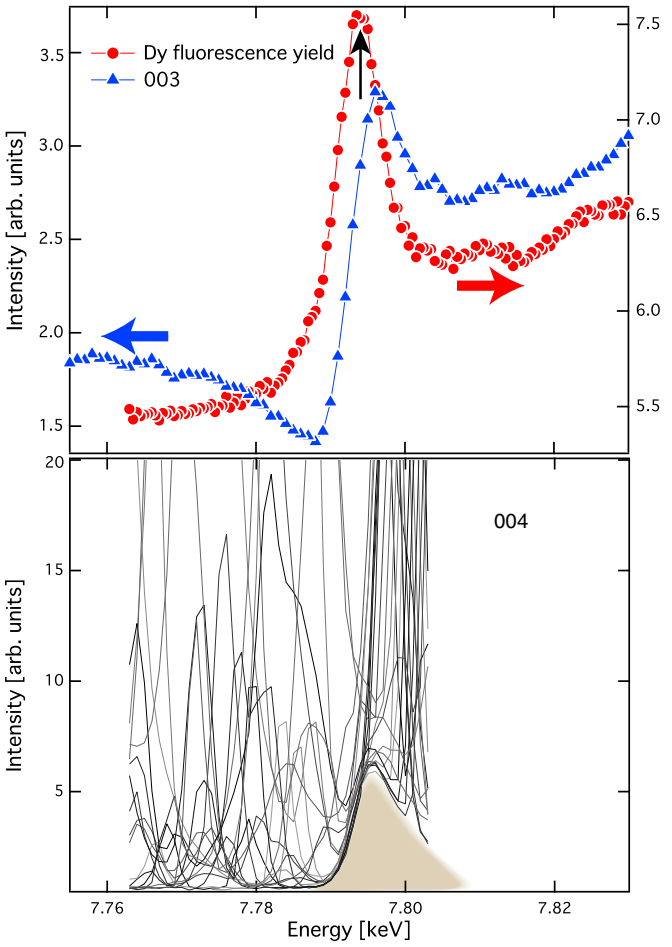

FIG. 3. Energy spectra of the x-ray absorption, the intensity of reflection 003, and that of forbidden reflection 004 around the Dy L_3 absorption edge. The data were observed at the beam line 3A in PF with the σ-polarized incident beam. Upper panel: the x-ray absorption spectrum obtained in the total fluorescence mode is shown by red circles and the intensity of reflection 003 is shown by blue triangles. The absorption effect is not corrected. The white line (the maximum absorption) is shown by a black arrow. Lower panel: the intensity of reflection 004 as a function of the x-ray energy was observed for the azimuth angle Ψ which was scanned in a range from 131.5° to 133.4° by every 0.1° step at $T = 200$ K. The resonant effect underlying in the intensity of reflection 004 is shaded around $E = 7.796$ keV.

in the top panels of Figs. 3 and 4, respectively. The XAS were observed by measuring the total fluorescence yield. The maximum absorption, the so-called white line, of the Dy L_3 edge and that of the Fe K edge was found to be at $E = 7.794$ and 7.125 keV, respectively, while the minimum intensity of reflection 003 around the Dy L_3 edge and around the Fe K edge was found at $E = 7.788$ and at 7.120 keV, respectively.

We have successfully observed space-group forbidden reflections 004 and 005 in the vicinity of both absorption edges. The intensity of these forbidden reflections is about an order of 10^{-4} to that of space-group allowed reflection 003. The resonant effect for the forbidden reflections is not easily specified by comparing the energy spectrum of reflection 003 with the XAS spectra, for both absorption edges. In order to observe the underlying resonant effect precisely,

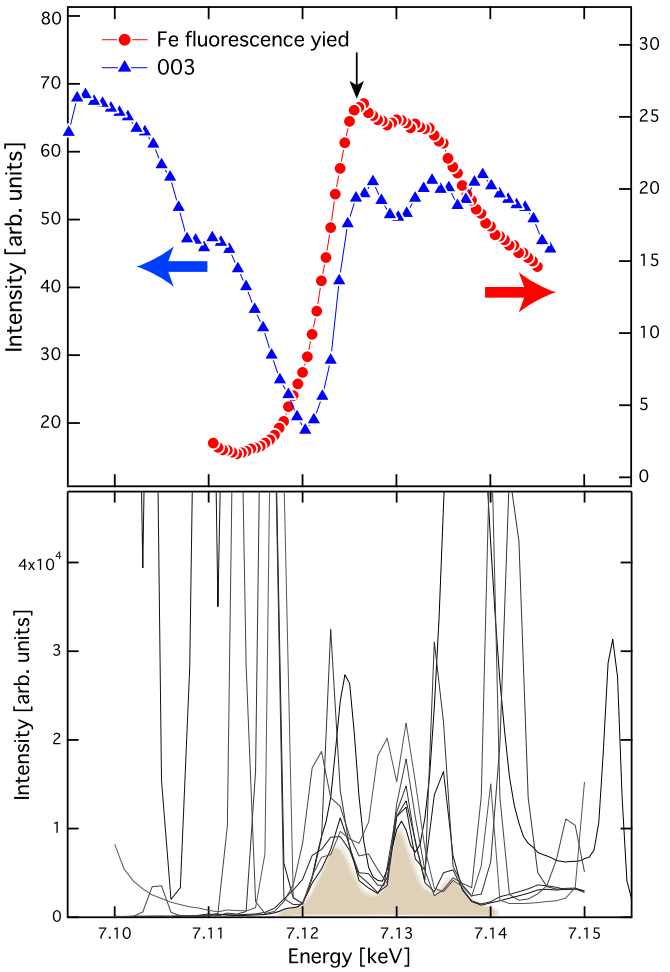

FIG. 4. Energy spectra of the x-ray absorption, reflection 003, and forbidden reflection 004 around the Fe K absorption edge. The data were observed at the beam line 29XUL in SPring-8 with the π-polarized incident beam. Upper panel: the x-ray absorption spectrum obtained in the total fluorescence mode is shown by red circles and the intensity of reflection 003 is shown by blue triangles. The absorption effect is not corrected. The white line (the maximum absorption) is shown by a black arrow. Lower panel: the intensity of reflection 004 as a function of the x-ray energy was observed for azimuth angles $\Psi = -100^\circ$, -105°, -110°, -114°, -115°, and -126° at $T =$ 50 K. The resonant effect underlying in the intensity of reflection 004 is shaded around $E = 7.13$ keV.

we performed energy scans for forbidden reflection 004 at several azimuth angles Ψ in a small range. The bottom panels of Figs. 3 and 4 show energy spectra of the intensity of reflection 004 around the Dy L_3 and the Fe K edges, respectively. As observed, reflection 004 is accompanied by strong multiple scattering effect or *Umweganregung* effect which adds apparently random bumpy structure to the spectra, which varies with the azimuth angle as well as the x-ray energy [25,26]. The underlying resonant enhancement is present under the intensity curves of reflection 004, which are bumpy due to the multiple scattering effect. The same method was used for deducing the Te L_1 resonant enhancement previously [13]. The enhancement for both absorption edges, observed as a single peak around $E = 7.796$ keV for the Dy L_3 edge and three peaks around $E = 7.13$ keV for the Fe K edge, is shown by the shaded areas in the bottom panels of Figs. 3 and 4, respectively. The feature of three peaks around Fe K absorption edge has been reported in the literature, for example, FeS_2 [27]. We employed $E = 7.796$ keV for the Dy L_3 absorption edge and $E = 7.13$ keV for the Fe K absorption edge in the following experiments.

B. Azimuth angle scans

We have performed azimuth angle scans for forbidden reflections 004 and 005 at $E = 7.796$ keV for the Dy L_3 absorption edge and $E = 7.13$ keV for the Fe K absorption edge with the positive and negative circularly polarized x-ray beams. We observed rocking curves at each fixed azimuth angle Ψ. The integrated intensity was numerically integrated, and a linear background due to the fluorescence was subtracted. Typical rocking curves are displayed in the insets of Figs. 5 and 6. The state of the x-ray polarization was manipulated by the diamond phase retarder for both absorption edges; the Stokes parameters are summarized in Table I. The values are given from the deviation angle in θ for Bragg reflection $2\bar{2}0$ of the diamond retarder. Here, $(+)$ and $(-)$ represent the helicity positive ($P_2 > 0$) and the helicity negative ($P_2 < 0$) states for the circularly polarized x-ray beam, respectively. Hereafter, we use symbols $(+)$ and $(-)$ for the positive and negative x-ray helicities, respectively. Because of an accidental inaccuracy for positioning the diamond phase retarder, we found that the P_3, the linear polarization, had unintended non-negligible values for both the positive and the negative circularly polarized x rays, while the P_1, the diagonal linear polarization, had negligible values. Accordingly, the values of P_2 are not exactly the same for both $(+)$ and $(-)$ states. This small deviation in P_2, however, does not matter for the following analysis for the quadrupole moment as we show later.

Figures 5 and 6 show the integrated intensity of reflections 004 and 005 for the $(+)$ and $(-)$ states and their difference intensity between two helicity states $(-)-(+)$ at Dy L_3 ($E = 7.796$ keV) absorption edge and at Fe K ($E = 7.13$ keV) absorption edge, respectively. All the data were measured at $T = 100$ K. The data are corrected with the experimental Lorentz factor. The absorption correction is not necessary because the incoming and outgoing beams have the same angle to the sample surface for both reflections. The range of azimuth angle Ψ for all scans is from -120° to 90°. The bumpy structure of azimuth scan curves is due to the multiple scattering effect as described in Sec. V A. The effect appears as a pair of data points for $(+)$ and $(-)$ circularly polarized states at the same Ψ point. Therefore, taking the difference between the two helicity states eliminates the multiple scattering effect and gives rather smooth azimuth curves for both reflections 004 and 005, and at both Dy L_3 and Fe K absorption edges. However, the subtraction cannot cancel out the multiple scattering effect completely because the degree of the linear polarization is different for the two circularly polarized states, as described in Table I.

We find that these azimuth functions have a 120° periodicity according to the trigonal crystal symmetry. Further, the intensity for the $(-)$ helicity is higher than that for the $(+)$ helicity for reflection 004 for both absorption edges, and

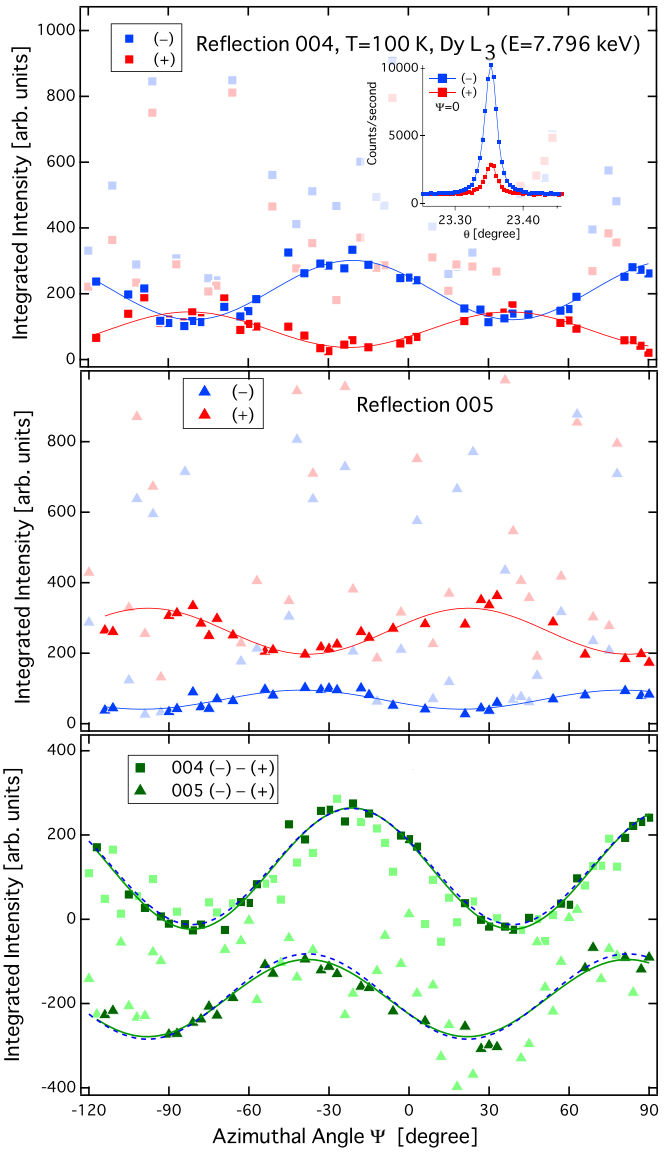

FIG. 5. The integrated intensity of forbidden reflections 004 (top panel) and 005 (middle panel) observed at the Dy L_3 absorption edge ($E = 7.796$ keV) and $T = 100$ K as a function of Ψ. The inset of the top panel shows rocking curves observed at $\Psi = 0$ for (+) and (−) helicity of the incident beam. Red squares (triangles) show the integrated intensity measured by the incident beam with the (+) helicity for reflection 004 (005) and blue squares (triangles) show that measured by the incident beam with the (−) helicity for reflection 004 (005). The bottom panel shows the difference intensity (−) − (+) between the two helicity states. The cosine curves are results of fit to the data with Eq. (14) for the top and middle panels, and fit to the data with Eq. (18) for the bottom panel. The points colored faintly are strongly influenced by the multiple scattering effect, and are removed for the fitting. The dashed lines in the bottom panel are given from the result of the least-squares method described in the text.

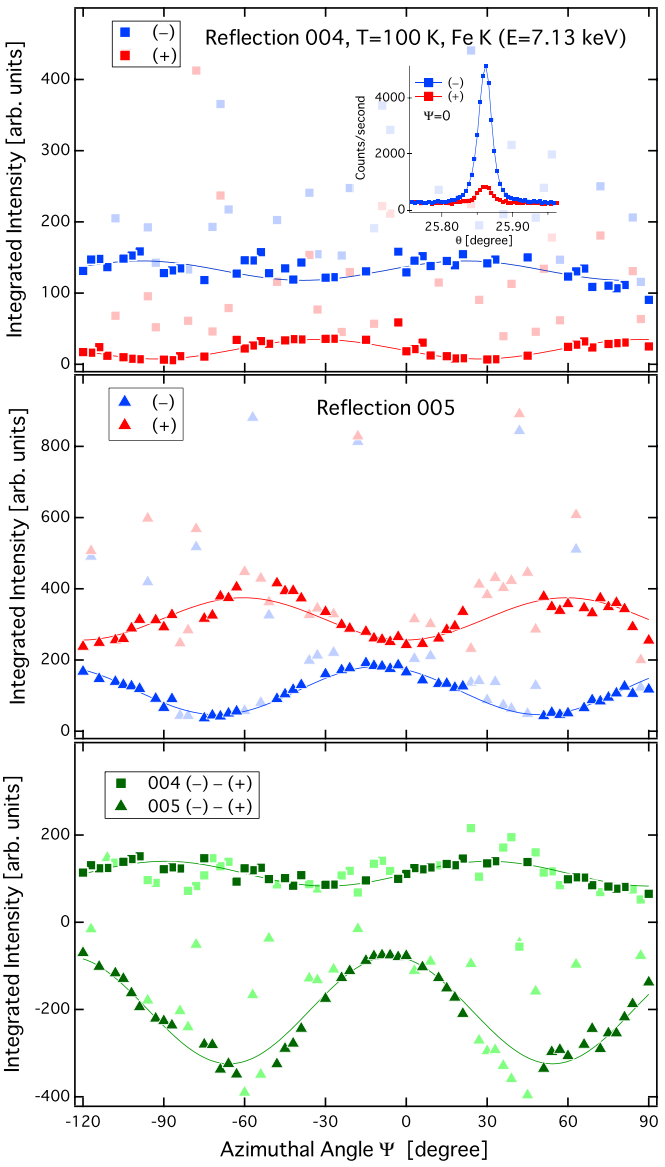

FIG. 6. The integrated intensity of forbidden reflections 004 (top panel) and 005 (middle panel) observed at the Fe K absorption edge ($E = 7.13$ keV) and temperature $T = 100$ K as a function of Ψ. The inset of the top panel shows rocking curves observed at $\Psi = 0$ for (+) and (−) helicity of the incident beam. Red squares (triangles) show the integrated intensity measured by the incident beam with the (+) helicity for reflection 004 (005) and blue squares (triangles) show that measured by the incident beam with the (−) helicity for reflection 004 (005). The bottom panel shows the difference intensity (−) − (+) between the two helicity states. The cosine curves are results of fit to the data with Eq. (14) for the top and middle panels, and fit to the data with Eq. (18) for the bottom panel. The points colored faintly are strongly influenced by the multiple scattering effect, and are removed for the fitting.

this relation is reversed for reflection 005. This fact exactly indicates that the sample used in this study belongs to the *left-handed* space group $P3_221$, as we confirm theoretically later. This handedness, of course, is in accord with our earlier study of soft x-ray diffraction at Dy M_5 absorption edge [16].

C. Temperature dependence

We analyzed the integrated intensity of forbidden reflection 004 observed at Dy L_3 and Fe K edges as a function of temperature. Figure 7 shows the integrated intensity of reflection 004 together with that of reflection 001 previously

TABLE I. The values of experimental Stokes parameters for two circularly polarized states (+) and (−) at Dy L_3 ($E = 7.796$ keV) and Fe K ($E = 7.13$ keV) absorption edges, together with the angle of the diamond crystal $\theta_{2\bar{2}0}$ for each polarization state.

		$\theta_{2\bar{2}0}$ (degree)	P_1	P_2	P_3
Dy L_3 7.796 keV	(+)	39.111	−0.0152	+0.978	−0.114
	(−)	39.073	+0.0139	−0.967	−0.203
Fe K 7.130 keV	(+)	43.612	−0.0195	+0.990	−0.023
	(−)	43.561	+0.0182	−0.986	−0.110

observed at Dy M_5 edge with a soft x-ray beam [16]. We measured the intensity at several azimuth angles, where the multiple scattering effect was expected to be negligible. The data shown here are observed at one fixed azimuth angle. We find that the temperature evolution of the integrated intensities of reflection 004 observed both at Dy L_3 and Fe K edges is quite different from that of reflection 001 observed at Dy M_5 edge. They show a rather monotonous increase on cooling after the jump just below the T_S while that of reflection 001 observed at Dy M_5 edge shows a steep increase towards lower temperatures. We discuss this feature comparing with the deformation of DyO_6 trigonal prism and FeO_6 octahedron in the next section.

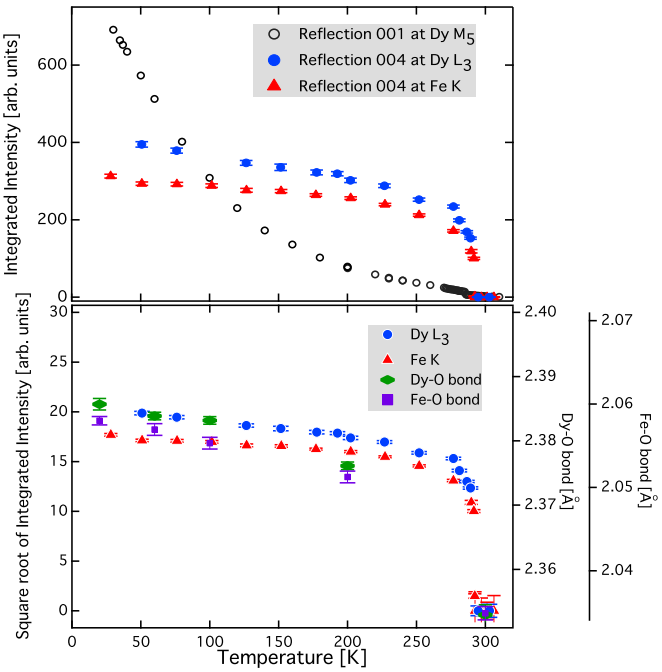

FIG. 7. The temperature dependence of the integrated intensity of ω scans for reflection 004. Top: the integrated intensity of reflection 004 observed at Dy L_3 absorption edge (circles) and Fe K absorption edge (triangles), and that for reflection 001 observed at Dy M_5 absorption edge (open circles) [16]. The integrated intensity of reflection 001 is multiplied by a factor to compare with the others. Bottom: the square root of the integrated intensity of reflection 004 observed at Dy L_3 absorption edge (circles) and Fe K absorption edge (triangles) together with the bond length of Dy-O(4) (diamonds) and the bond length of Fe(2)-O(2_1) (squares) [16].

VI. DISCUSSION AND ANALYSIS

A. Dy 5*d* and Fe 4*p* quadrupole moments in the azimuth scans

The intensity I of the resonant diffraction is generally given with the Stokes parameters [28]

$$\begin{aligned} I = {} & \tfrac{1}{2}(1+P_3)(|G_{\sigma'\sigma}|^2 + |G_{\pi'\sigma}|^2) \\ & + \tfrac{1}{2}(1-P_3)(|G_{\pi'\pi}|^2 + |G_{\sigma'\pi}|^2) \\ & + P_2 \mathrm{Im}(G^*_{\sigma'\pi} G_{\sigma'\sigma} + G^*_{\pi'\pi} G_{\pi'\sigma}) \\ & + P_1 \mathrm{Re}(G^*_{\sigma'\pi} G_{\sigma'\sigma} + G^*_{\pi'\pi} G_{\pi'\sigma}). \end{aligned} \quad (4)$$

Here, $G_{\alpha'\beta}$ is the total resonant scattering amplitude, and α' and β are the polarization states of the diffracted and incident x-ray beam, respectively. The third term including P_2 represents the interference between σ and π components in the resonant scattering process for the circularly polarized x rays. It plays a crucial role for determination of the chirality by changing the sign coupling with the helicity of the x-ray beam.

We use the atomic multipoles $\langle T^K_Q \rangle$, the expectation value of the spherical tensor, to express the scattering amplitude $G_{\alpha'\beta}$ as described in Ref. [28]. This method is very useful for discussing the components of the multipole moment ordered in materials. The total scattering amplitude is composed of possible resonant events

$$G_{\alpha'\beta} = \sum_k r^{(k)} \frac{F^{(k)}_{\alpha'\beta}}{\hbar\omega - \Delta + \frac{i}{2}\Gamma} = \sum_k d^{(k)}(E) F^{(k)}_{\alpha'\beta}, \quad (5)$$

where k represents individual resonant events like $E1E1$, $E1E2$, etc., Δ, Γ, and $r^{(k)}$ represent the resonant energy, its width, and the mixing parameter, respectively, and the scattering length $F_{\alpha'\beta}$ is

$$F_{\alpha'\beta} = \sum_K X^{(K)}_{\alpha'\beta} D^{(K)} \Psi^{(K)}. \quad (6)$$

Here, $\Psi^{(K)}$ represents the unit-cell structure-factor tensor of rank K which is the sum of atomic multipoles related to the resonant process, and $X^{(K)}_{\alpha'\beta}$ describes the conditions of the incident and the diffracted beams. Orientation of the crystal, with respect to states of polarization and the plane of scattering, is accomplished by a rotation matrix $D^{(K)}$. Note that the atomic scattering length expressed by Eq. (2) is summed up in the unit-cell structure factor $\Psi^{(K)}$ including the geometric factor $X^{(K)}_{\alpha'\beta} D^{(K)}$, and that the tensorial character is linked with the x-ray polarization.

As far as the Dy $4f$ and $5d$ quadrupole moments are concerned, the structure factor for the enantiomorphic space-group pair $P3_121$ (No. 152) and $P3_221$ (No. 154) described in Ref. [12] is applicable to $DyFe_3(BO_3)_4$ because the Dy site is at the special position $3a$ (multiplicity 3 and Wyckoff letter a), which is the same as the Si site in low quartz. For the space groups No. 152 and No. 154, Dy ions locate at $(x, 0, \pm\frac{1}{3})$, $(0, x, \mp\frac{1}{3})$, and $(-x, -x, 0)$ in a unit cell. Here, the upper and lower signs represent the space groups No 152 and No. 154, respectively. The unit-cell structure factor is the sum of the atomic multipoles, each of which is defined at each Dy ion. First, we define the atomic multipole $\langle T^K_Q \rangle$ at the ion $(-x, -x, 0)$, which is common for both space groups, with a right-handed Cartesian axis $(\xi\eta\zeta)$. Here, the ζ axis

is parallel to the c axis, and the ξ axis parallel to the [1, 1, 0] axis, which encloses an angle of 30° with the reciprocal a^* axis. The atomic multipoles of the other Dy ions at (x, 0, $\pm\frac{1}{3}$) and (0, x, $\mp\frac{1}{3}$) are given as $\langle T_Q^K\rangle \exp(2\pi i Q/3)$ and $\langle T_Q^K\rangle \exp(-2\pi i Q/3)$, respectively, with a rotation along the ζ axis by +120° and −120°, respectively. The unit-cell structure factor for reflection 00l is

$$\Psi_Q^K = \langle T_Q^K\rangle\{1 + e^{2\pi i Q/3}e^{2\pi i(\pm l/3)} + e^{-2\pi i Q/3}e^{2\pi i(\mp l/3)}\}. \quad (7)$$

Here, we find the selection rule for reflection 00l that $l + Q = 3n$ for space group $P3_121$ and $l - Q = 3n$ for space group $P3_221$, where n is an integer. The handedness emerges as the sign of Q.

The most probable resonant process at the Dy at L_3 absorption edge is the $E1E1$ event, the resonance between $2p_{\frac{3}{2}}$ and $5d$. As we discuss later, the asymmetric process $E1E2$ is negligible. The atomic multipole related to the $E1E1$ event is $\langle T_Q^K\rangle$ with rank $K = 2$, in other words, the quadrupole. There are five independent components for the quadrupole moment with relations $\langle T_{+1}^2\rangle' = -\langle T_{-1}^2\rangle'$, $\langle T_{+1}^2\rangle'' = \langle T_{-1}^2\rangle''$, $\langle T_{+2}^2\rangle' = \langle T_{-2}^2\rangle'$, and $\langle T_{+2}^2\rangle'' = -\langle T_{-2}^2\rangle''$. Note that the atomic multipole $\langle T_Q^K\rangle$ is a complex number defined as $\langle T_Q^K\rangle = \langle T_Q^K\rangle' + i\langle T_Q^K\rangle''$ with $\langle T_Q^K\rangle^* = (-1)^Q\langle T_{-Q}^K\rangle$. The five independent components are real numbers: $\langle T_0^2\rangle'$, $\langle T_{+1}^2\rangle'$, $\langle T_{+1}^2\rangle''$, $\langle T_{+2}^2\rangle'$, and $\langle T_{+2}^2\rangle''$, each of which corresponds to $3\zeta^2 - r^2$, $\zeta\xi$, $\eta\zeta$, $\xi^2 - \eta^2$, and $\xi\eta$ components, respectively. Among the five components, $\langle T_{+1}^2\rangle'$, and $\langle T_{+2}^2\rangle''$ are zero for the Dy ions because the site a is on the twofold axis which gives the relation $\langle T_Q^K\rangle = (-1)^K\langle T_{-Q}^K\rangle$. The selection rule $l \pm Q = 3n$ for space-group forbidden reflections 00l ($l \neq 3n$) excludes the $\langle T_0^2\rangle'$ component. Therefore, as far as $E1E1$ process is concerned at Dy L_3 edge, the intensity of space-group forbidden reflections is described by only two components $\langle T_{+2}^2\rangle'$, and $\langle T_{+1}^2\rangle''$. Note that the mirror operation between enantiomorphic space-group pair No. 152 and No. 154 gives

$$\langle T_{+1}^2\rangle''_{\text{No. 152}} = -\langle T_{+1}^2\rangle''_{\text{No. 154}}, \quad (8)$$

$$\langle T_{+2}^2\rangle'_{\text{No. 152}} = \langle T_{+2}^2\rangle'_{\text{No. 154}}. \quad (9)$$

Equation (9) shows that the component on the basal plane is common for both of the enantiomorphic space-group pair, while Eq. (8) shows that the component on the $\eta\zeta$ plane has the opposite sign to each other. The four amplitudes [12] for space-group forbidden reflections 00l, $l = 3n + \mu$ ($\mu = \pm 1$) for the parity-even event $E1E1$ at Dy L_3 absorption edge, are

$$G_{\sigma'\sigma} = \tfrac{3}{2}\langle T_{+2}^2\rangle' e^{i\phi_a}, \quad (10)$$

$$G_{\pi'\pi} = \tfrac{3}{2}\langle T_{+2}^2\rangle' e^{i\phi_a}\sin^2\theta, \quad (11)$$

$$G_{\pi'\sigma} = \tfrac{3}{2}i\lambda\{\langle T_{+2}^2\rangle' e^{i\phi_a}\sin\theta + \langle T_{+1}^2\rangle'' e^{i\phi_b}\cos\theta e^{3i\lambda\Psi}\}, \quad (12)$$

$$G_{\sigma'\pi} = \tfrac{3}{2}i\lambda\{-\langle T_{+2}^2\rangle' e^{i\phi_a}\sin\theta + \langle T_{+1}^2\rangle'' e^{i\phi_b}\cos\theta e^{3i\lambda\Psi}\}. \quad (13)$$

Here, Bragg angle θ and the azimuth angle Ψ are shown and defined in Fig. 2. The phase factors $e^{i\phi_a}$ and $e^{i\phi_b}$ emerge from Eq. (5), and depend on the x-ray energy differently to each other [29,30]. Here, we introduce two parameters $\nu = \pm 1$ and $\lambda = \pm 1$. The parameter ν denotes the crystal handedness, namely, $\nu = +1$ for the right-handed space group No. 152, and $\nu = -1$ for the left-handed space group No. 154, and the parameter λ denotes the product of μ and ν, $\lambda = \mu\nu$. Note that the rotating direction of Ψ is opposite to that defined in Ref. [12].

The intensity I for the $E1E1$ event at Dy L_3 absorption edge is

$$I = I_0 + I_1\cos 3(\lambda\Psi + \phi), \quad (14)$$

$$I_0 = \tfrac{1}{2}\{(1 + \sin^2\theta)^2 T_a^2 + 2\cos^2\theta\, T_b^2 + P_3(1 + \sin^2\theta) \times \cos^2\theta\, T_a^2\} + \lambda P_2\sin\theta\big(1 + \sin^2\theta\big)T_a^2, \quad (15)$$

$$I_1 = \big(2P_3\sin\theta\cos\theta - \lambda P_2\cos^3\theta\big)T_aT_b. \quad (16)$$

Here, we define the parameters $\phi = \frac{1}{3}(\phi_b - \phi_a)$, $T_a = \frac{3}{2}\langle T_{+2}^2\rangle'$, $T_b = \frac{3}{2}\langle T_{+1}^2\rangle''$, and we presume $P_1 = 0$ for simplicity. Equations (14)–(16) are the same as those of Ref. [12] in the $E1E1$ transition except for the presence of the shift ϕ in Ψ. The intensity is a threefold periodic function of the azimuthal angle Ψ. The circular polarization P_2 is multiplied by λ, indicating that reversing the crystal chirality ν together with reversing the sign of circular polarization does not change the intensity. Only the shift ϕ in Ψ changes its sign with λ according to Eq. (14). The relation of Eq. (8) is absorbed in T_b itself in Eq. (16). By extracting it, we find

$$I_1 = (2\nu P_3\sin\theta\cos\theta - \mu P_2\cos^3\theta)T_aT_b, \quad (17)$$

with $T_b = T_{b(\text{No. 152})} = -T_{b(\text{No. 154})}$. Equation (17) gives relations (i) $I_1(+\nu, \pm P_2) = -I_1(-\nu, \mp P_2)$ for the same reflection index, (ii) when $P_3 = 0$, $I_1(+\nu, \pm P_2) = I_1(-\nu, \pm P_2)$ for the same reflection index, and (iii) when $P_3 = 0$, I_1 for reflection indices $\mu = +1$ and $\mu = -1$ has the opposite sign to each other for the same values of ν and P_2. The previous observations for $DyFe_3(BO_3)_4$ and low quartz [11,16,29] support the relation (i), and also suggest the relation (ii) for the small value of P_3. The relation (iii) has been confirmed in the data sets of Te and $AlPO_4$ [13,14]. The difference intensity between two helicity states ($P_2 = -1$ and $+1$) is

$$I(-) - I(+) = A + B\cos 3(\lambda\Psi + \phi), \quad (18)$$

with $A = -2\lambda\sin\theta(1 + \sin^2\theta)T_a^2$ and $B = 2\mu\cos^3\theta\, T_aT_b$. Note that there are only two quadrupole components T_a and T_b for the intensity at Dy L_3 absorption edge.

Analyzing the Fe $4p$ quadrupole moments observed at the Fe K absorption edge is more complicated because there are nine ions in a unit cell: three of them, Fe(1), are at the special position $3a$ (multiplicity 3, Wyckoff letter a) and the other six, Fe(2), are at the general position $6c$ (multiplicity 6, Wyckoff letter c) in the low-T phase. For 00l reflection, six independent $4p$ quadrupole components contribute in total: they are two quadrupole components of three Fe(1) ions,

$$Q_{\xi^2-\eta^2}^{(1)} = \langle T_{+2}^2\rangle'^{(1)}e^{ip_1},$$

$$Q_{\eta\zeta}^{(1)} = \langle T_{+1}^2\rangle''^{(1)}e^{iq_1},$$

and four quadrupole components of six Fe(2) ions,

$$Q^{(2)}_{\xi^2-\eta^2} = \langle T^2_{+2}\rangle'^{(2)} e^{ip_2},$$
$$Q^{(2)}_{\xi\eta} = \langle T^2_{+2}\rangle''^{(2)} e^{iq_2},$$
$$Q^{(2)}_{\eta\zeta} = \langle T^2_{+1}\rangle''^{(2)} e^{ir_2},$$
$$Q^{(2)}_{\zeta\xi} = \langle T^2_{+1}\rangle'^{(2)} e^{is_2}.$$

The components are defined with the local coordinate $(\xi\eta\zeta)$ in the same way as Dy components. Each component is a complex number and has an independent phase factor according to Eq. (5). When $P_1 = 0$, we obtain the intensity of forbidden reflection $00l$ at Fe K edge

$$I = I_0 + I_1 \cos 3(\lambda\Psi + \phi), \tag{19}$$

$$I_0 = \tfrac{1}{2}\{(1+\sin^2\theta)^2 T^2_\alpha + 2\cos^2\theta\, T^2_\beta + P_3(1+\sin^2\theta) \times \cos^2\theta\, T^2_\alpha\} + \lambda P_2 \sin\theta(1+\sin^2\theta)T^2_\alpha, \tag{20}$$

$$I_1 = (2\nu P_3 \sin\theta\cos\theta - \mu P_2 \cos^3\theta)T_\alpha T_\beta, \tag{21}$$

with

$$T_\alpha e^{i\phi_\alpha} = 3\left\{\frac{(-1)^l}{2} Q^{(1)}_{\xi^2-\eta^2} + \cos\rho\, Q^{(2)}_{\xi^2-\eta^2} - \mu\sin\rho\, Q^{(2)}_{\xi\eta}\right\}, \tag{22a}$$

$$T_\beta e^{i\phi_\beta} = 3\left\{\frac{(-1)^l}{2} Q^{(1)}_{\eta\zeta} + \cos\rho\, Q^{(2)}_{\eta\zeta} + \mu\sin\rho\, Q^{(2)}_{\zeta\xi}\right\}. \tag{22b}$$

Here, $\phi = \frac{1}{3}(\phi_\beta - \phi_\alpha)$ and $\rho = 2\pi l(\frac{1}{6} - \delta)$. We define δ as $0.323\,33 = 1/3 - \delta$, and $\delta = 0.010\,003$ for one of the Fe(2) ions, which is located at (0.549 06, 0.335 907, 0.323 33) in a unit cell. Note that the parameters T_α and T_β are real numbers. As we see, Eqs. (20) and (21) have the same form as Eqs. (15) and (17), respectively, and are obtained by replacing T_a and T_b with T_α and T_β. Therefore, we employ the same functions to analyze the azimuth-angle-scan data sets for Dy L_3 and Fe K absorption edges.

We fit the data sets of the azimuth angle scans shown in Figs. 5 and 6 for the integrated intensity of two helicity states ($P_2 < 0$ and $P_2 > 0$) with Eq. (14), and for difference intensity $I(-) - I(+)$ with Eq. (18), together with the origin shift ϕ in Ψ. In practice, the fitting was carried out with selected data points to make a cosine envelope curve for each data set, otherwise, the multiple scattering prevents us from fitting properly. The multiple scattering generally raises the intensity steeply. However, an envelope shape is visible by connecting the minimum intensity points, which seem to be less affected by the multiple scattering, for each azimuth-angle-scan profile. We exclude pairs of data points, when both of them have clearly higher intensities compared to the envelope lines, for the (+) and (−) helicity states at the same Ψ points. Looking at the data carefully, we find that at some Ψ points, only one out of the pair seems to deviate from the envelope lines. The reason is not clear, but we believe that the effect of the multiple scattering is quite sensitive to the measurement condition simply because the intensity of the multiple scattering is extremely high compared to the forbidden reflections. Such a deviation might be due to the difference of the degree of the linear polarization for the two circularly polarized states as described in Table I or an unknown error in the measurement. We exclude those data points, even when one out of the pair deviates from the envelope lines, for the analysis of the subtraction data sets. Moreover, we find that some data points fall below the envelope lines for reflection 005 in both Figs. 5 and 6. As reported in the literature, for example Ref. [27], the interference between the resonant scattering and the multiple scattering makes an asymmetric feature for the Ψ profile, and lowers the intensity within a very small region of Ψ in the vicinity of the multiple scattering. We also exclude the points whose intensity seems to be coincidently lowered by the interference effect described above. Some arbitrariness is inevitable for this selection, however, each curve shown in Figs. 5 and 6 traces the envelope shape in each data set very well. The results of the fits are summarized in Table. II. The points colored faintly in both figures have been removed for the fitting.

We find that parameter A is positive for reflection 004 and is negative for reflection 005 at Dy L_3 absorption edge, which indicates that $\nu = -1$, i.e., the sample we observed belongs to the left-handed space group No. 154. This is consistent with the previous observation at the Dy M_5 edge [16]. Likewise, the parameter A for the data observed at the Fe K edge is positive and the same discussion is applicable to the handedness of the Fe structure in this sample. Of course, the handedness of the Dy structure and the Fe structure is coincident in the same space group. Moreover, we find that the relation (iii) for I_1 in Eq. (17) is confirmed between reflections 004 and 005 at both

TABLE II. The values of the parameters as results of fit to the data sets of the azimuth angle scans for reflections 004 and 005 shown in Figs. 5 and 6. Two helicity states ($P_2 < 0$ and $P_2 > 0$) are represented by (−) and (+), respectively. The data sets are fit by Eqs. (14) with parameters I_0, I_1, and ϕ and the subtracted data $I(-) - I(+)$ are fit by Eq. (18) with parameters A, B, and ϕ.

		Dy L_3 edge			Fe K edge		
	Helicity (P_2)	$I_0(A)$	$I_1(B)$	ϕ	$I_0(A)$	$I_1(B)$	ϕ
004	(−)	211.2 ± 4.2	−90.1 ± 5.6	39.1 ± 1.3	131.3 ± 1.4	−14.7 ± 1.9	−33.7 ± 2.8
	(+)	90.9 ± 3.7	53.9 ± 5.0	37.8 ± 1.9	21.2 ± 0.5	13.7 ± 0.8	−32.9 ± 1.2
	(−) − (+)	120.3 ± 3.3	−143.9 ± 3.8	38.6 ± 0.6	109.1 ± 1.5	−26.5 ± 1.9	−33.7 ± 1.7
005	(−)	68.2 ± 2.3	27.1 ± 3.3	40.1 ± 2.4	114.0 ± 1.5	67.7 ± 2.2	10.2 ± 0.6
	(+)	262.3 ± 5.2	−65.2 ± 6.8	37.9 ± 2.2	315.4 ± 4.9	−59.4 ± 6.9	0.6 ± 2.2
	(−) − (+)	−187.1 ± 3.8	91.6 ± 5.0	38.1 ± 1.2	−201.4 ± 3.2	123.0 ± 5.8	5.7 ± 0.9

absorption edges, and that the origin shift ϕ in Ψ is almost unchanged for both the helicity states (−) and (+) at the Dy M_5 edge, which evidences that the $E1E1$ process is also valid for the experimental data at the Dy L_3 edge. The discrepancy in ϕ about 12° between two helicity states has been found in the study of low quartz [11]. This discrepancy has been discussed in terms of the birefringence phenomenon, higher-order transition processes like $E1E2$, or the x-ray polarization itself [29]. Finally, it has been concluded that a tiny but non-negligible off-diagonal polarization P_1 possibly causes such discrepancy, and that the effects of higher-order transition processes and the birefringence should be very small, judging from the *ab initio* simulation and the x-ray absorption near-edge spectroscopy (XANES) experimental data. Present data sets do not show any obvious discrepancy in ϕ between two helicity states for both reflections 004 and 005 at Dy L_3 edge. The same discussion is applicable to the origin shift ϕ in Ψ for the data observed at the Fe K edge. The values of ϕ are almost the same for both two helicity states (−) and (+) for reflection 004, although there is some deviation for reflection 005. Note that in case of Fe K edge, the origin shifts ϕ for reflections 004 and 005 are not necessarily coincident. Equation (22) shows that six independent Fe $4p$ quadrupole components are summed up in two parameters, T_α and T_β, both of which depend on the reflection index with the interference between these sites. Consequently, the scattering amplitude does not necessarily have the same value of ϕ for reflections 004 and 005, although the circular polarization does not change ϕ.

Let us discuss about the quadrupole moments with the experimental data. Analyzing the Dy $5d$ quadrupole moments is easy because there are only two parameters $\langle T^2_{+2}\rangle'$ and $\langle T^2_{+1}\rangle''$ in four equations. On the other hand, it is not easy for the Fe $4p$ quadrupole moments because there are six parameters summed up in Eq. (22). We escape to deduce anything about the Fe $4p$ quadrupoles because of the complexity.

Hereafter, we discuss the Dy $5d$ quadrupoles. In case of pure circularly polarized states ($P_2 = -1$ and $P_2 = +1$), Eq. (14) is applicable to solve the parameters. However, in practice, the experimental Stokes parameters described in Table I are not simple because P_3 has non-negligible values. In order to solve the parameters, we applied the least-squares method described in the Appendix A for the equations used to describe reflections 004 and 005. The results are $|\langle T^2_{+2}\rangle'| = 7.77 \pm 0.06$ and $|\langle T^2_{+1}\rangle''| = 5.20 \pm 0.15$ for the Dy $5d$ quadrupole moment. The ratio is $r = |\langle T^2_{+1}\rangle''/\langle T^2_{+2}\rangle'| = 0.67 \pm 0.02$. We find that the dashed lines at the bottom panel of Fig. 5 given by these values are quite similar to the lines obtained from the independent fits by Eq. (18). Note that the absolute values are meaningless, only the ratio has a meaning, and that we cannot determine the signs of these components because the phase shift ϕ has arbitrariness of 60° (a half period in Ψ), accompanied with the sign of I_1.

As reported in Ref. [16], the ratio $r = |\langle T^2_{+1}\rangle''/\langle T^2_{+2}\rangle'|$, or $r = (\eta\zeta)/(\xi^2 - \eta^2)$ for simplicity, for the Dy $4f$ quadrupole is close to unity. It changes from 0.9 at 200 K to 1.23 at 50 K as temperature decreases. Since the Dy $4f$ states are spatially localized, it is presumed that the ratio is close to unity and that the change with temperature is due to electrostatic effect by the crystal electric field. On the other hand, we find that the ratio of the Dy $5d$ quadrupole components is 0.67 [$= (\eta\zeta)/(\xi^2 - \eta^2)$] at 100 K. The value clearly deviates from unity. This deviation is probably due to the bonding between the Dy $5d$ state and the oxygen $2p$ state. At present, however, it is difficult to give a clear explanation for this value because the deformation of the DyO_6 prism is complicated as described in the following subsection. A precise calculation of the electron density around the Dy ion coupling with the oxygen ligands is required to explain the Dy $5d$ state.

B. Deformation of DyO_6 trigonal prism and FeO_6 octahedron as a function of temperature

According to the previous crystal structure analysis [16], the structural phase transition lowers the site symmetry of Dy, which is on the threefold rotation axis in the high-T $R32$ phase, with a translational shift along the twofold axis and a deformation of the DyO_6 trigonal prism: the Dy-O(4) bond elongates and the Dy-O(3) and Dy-O(7) bonds shrink at $T < T_S$ while the six oxygen atoms are equidistant from the central Dy ion at $T > T_S$. Accordingly, the site symmetry of Dy changes from D_3 to C_2, losing the threefold symmetry in the low-T $P3_121$ or $P3_221$ phase. Here, the number after the chemical symbol indicates the site position in the atomic coordinate determined by the single-crystal x-ray diffraction measurements, of which information is provided in the supplementary information of Ref. [16].

Likewise, the FeO_6 octahedron deforms in the low-T phase. The Fe ions are located at site $9d$, which is at the site symmetry C_2: one of the three twofold axes perpendicular to the c axis, in the high-T $R32$ phase. As described in the previous section, in the low-T phase, the nine Fe ions are separated into two groups: three Fe(1) ions are at the special position $3a$, remaining on one of three twofold axes, and six Fe(2) ions are at the general position $6c$. Figure 8 illustrates the deformation of the DyO_6 trigonal prism and Fe(1)O_6, Fe(2)O_6 octahedrons. Here, pair bonds Dy-O(3), Dy-O(4), and Dy-O(7) in the DyO_6, and

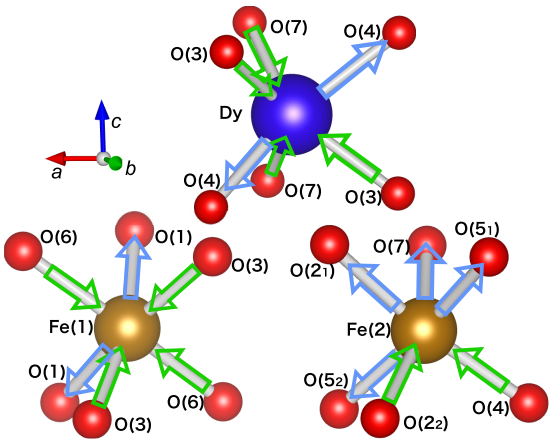

FIG. 8. An image of deformation in a DyO_6 trigonal prism and two FeO_6 octahedra in the low-T $P3_221$ phase due to the structural phase transition at T_S. This image is drawn by VESTA [34]. Here, the Fe(1) ion locates at $3a$ site and the Fe(2) ion locates at $6b$ site in the low-T $P3_221$ phase. The arrows show the direction of the elongation or the shrinkage. Pair bonds Fe(2)-O(2) lose the symmetry and that the Fe(2)-O(2_1) bond elongates and the other Fe(2)-O(2_2) bond shrinks.

Fe(1)-O(1), Fe(1)-O(3), and Fe(1)-O(6) in $Fe(1)O_6$ are equidistant, respectively, in the low-T phase so as that Dy and Fe(1) ions are kept to be on the twofold axes perpendicular to the c axis, whereas all six bonds Fe(2)-O in $Fe(2)O_6$ octahedron are different from each other.

We show the deformation of the DyO_6 trigonal prism and $Fe(1)O_6$, $Fe(2)O_6$ octahedrons as a function of temperature by taking two typical bonds Dy-O(4) and Fe(2)-O(2_1) in the bottom panel of Fig. 7 together with the square root of the integrated intensity of reflection 004 observed at two absorption edges Dy L_3 and Fe K. As seen, we find that the square root of the integrated intensity shows a monotonous change with temperature as well as the lengths of two bonds Dy-O(4) and Fe(2)-O(2_1), indicating that the Dy $5d$ quadrupole moment strongly couples with ligand oxygen atoms. On the other hand, the integrated intensity of reflection 001 at Dy M_5 edge shows a drastic increase with decreasing temperature, indicating that the development of the Dy $4f$ quadrupole moment is independent of the deformation of the DyO_6 trigonal prism. This development is possibly caused by the population at the respective sublevels in eight Kramers doublets in the ${}^6H_{\frac{15}{2}}$ state of Dy^{+3} $4f$ electrons. Note that the splitting energy between the first and the second sublevels is estimated to be $15 \sim 20\,\mathrm{cm}^{-1}$ [23,31–33]. The observed different temperature dependence of the Dy $5d$, Fe $4p$, and Dy $4f$ quadrupole moments is explicitly attributed to the different degree of localization of these states. While the Dy $4f$ states are spatially fully localized and experience the atomic surroundings only electrostatically by the crystal electric field, the Dy $5d$ and Fe $4p$ states are directly involved in chemical bonding.

VII. CONCLUSION

We have investigated the quadrupole moments of Dy $5d$ and Fe $4p$ electrons in $DyFe_3(BO_3)_4$ which has the chiral helix structure of Dy and Fe ions on the screw axes. We have performed resonant x-ray diffraction with circularly polarized x rays at Dy L_3 and Fe K absorption edges by switching the sign of the x-ray helicity. The integrated intensity of forbidden reflections 004 and 005 has been observed as a function of azimuth angle Ψ and temperature.

The integrated intensity of the diffracted beam is theoretically interpreted well: (i) the periodicity of azimuth angle scan is 120°, which agrees with crystal symmetry, (ii) the helicity of circular polarization changes the intensity according to the crystal handedness, (iii) the phase shift ϕ in azimuthal scan is unchanged for both two helicity states (−) and (+) of the x-ray beam at Dy L_3 and Fe K edges, (iv) the intensity at Dy L_3 edge is described by two components of the Dy $5d$ quadrupole, (v) on the other hand, that at Fe K edge is described by totally six components of the Fe $4p$ quadrupoles for three Fe ions at the special position $3a$ and six Fe ions at the general position $6c$.

From the results (i) and (ii), we find that the crystal which we studied belongs to the left-handed space group $P3_221$, and this is in accord with our earlier results on soft x-ray diffraction at Dy M_5 absorption edge [16]. The result (iii) evidences that the resonant processes at both Dy L_3 and Fe K edges are well described within the scheme of $E1E1$ process, and that the birefringence phenomenon, or higher-order transition processes like $E1E2$, are unnecessary to be considered for the analysis of the experimental data. The discrepancy of the phase shift ϕ between reflections 004 and 005 observed at Fe K edge is theoretically predicted by the admixture of Fe $4p$ quadrupole moments at two sites.

From the result (iv), we have determined the ratio of two components of the Dy $5d$ moment at $T = 100$ K as $r = |\langle T^2_{+1}\rangle''/\langle T^2_{+2}\rangle'| = 0.67 \pm 0.02$, which is smaller than $r = 1.20$ for the Dy $4f$ moment [16]. The temperature dependence of the diffracted intensity shows a rather monotonous increase on cooling after the jump just below the T_S, while that of reflection 001 observed at Dy M_5 edge shows a steep increase towards lower temperatures. These results indicate that the Dy $4f$ moment is less coupled with ligand oxygen atoms than the Dy $5d$ moment.

ACKNOWLEDGMENTS

It is a pleasure to acknowledge important discussions with M. Takahashi. We thank A. Chainani for his advice on the language. This work was supported by Grants-in-Aid for Scientific Research Grants No. 24244058 and No. and 25247054, MEXT, Japan. Resonant x-ray diffraction experiments were performed at beam lines 29XUL and 17SU in SPring-8 (RIKEN Proposals No. 20120019 and No. 20130066) and beam line 3A in the Photon Factory (Proposal No. 2014S2-003).

APPENDIX: CALCULATION FOR THE COMPONENTS OF DY $5d$ MOMENT USING THE LEAST-SQUARES METHOD

The experimental x-ray polarization was not purely defined as $P_1 = P_3 = 0$, $P_2 = \pm 1$. We use the values of P_2 and P_3 summarized in Table I for the analysis. The value of P_1 is negligible. There are two experimental parameters $p = \frac{9}{4}\langle T^2_{+2}\rangle'^2$ and $q = \frac{9}{4}\langle T^2_{+2}\rangle'\langle T^2_{+1}\rangle''$. The difference of the integrated intensities ΔI between two helicity states is

$$\begin{aligned}
\Delta I &= \Delta I_0 + \Delta I_1 \cos 3(\lambda\Psi + \phi),\\
\Delta I_0 &= I_0^- - I_0^+\\
&= \left\{\tfrac{1}{2}(P_3^- - P_3^+)\cos^2\theta + \lambda(P_2^- - P_2^+)\sin\theta\right\}\\
&\quad \times (1 + \sin^2\theta)\, p,\\
\Delta I_1 &= I_1^- - I_1^+\\
&= \left\{2(P_3^- - P_3^+)\sin\theta - \lambda(P_2^- - P_2^+)\cos^2\theta\right\}\\
&\quad \times \cos\theta\, q. \qquad \text{(A1)}
\end{aligned}$$

Here, the suffixes "+" and "−" represent the positive $P_2 > 0$ and negative $P_2 < 0$ helicities, respectively. The sum of the squares of the difference between the experimental data and the theoretical functions for reflections 004 and 005 is

$$\Delta = ({}^{\exp}\Delta I_{004} - {}^{\mathrm{cal}}\Delta I_{004})^2 + ({}^{\exp}\Delta I_{005} - {}^{\mathrm{cal}}\Delta I_{004})^2. \quad \text{(A2)}$$

Here, the prefixes "exp" and "cal" represent the experimental data set selected for the fit and Eq. (A1) including parameters p and q, respectively. The least-squares method is carried out to make the sum Δ minimum. This is a simple linear-least-squares calculation, and the values of p and q are directly obtained. Finally, we find that $p = 135.7 \pm 2.14$ and $q = 90.8 \pm 2.46$, and that the components of the Dy $5d$ quadrupole

are $|\langle T^2_{+1}\rangle|'' = 5.20 \pm 0.15$, $|\langle T^2_{+2}\rangle|' = 7.77 \pm 0.061$, and $r = |\langle T^2_{+1}\rangle''/\langle T^2_{+2}\rangle'| = 0.67 \pm 0.02$. Note that the sign of each component is undetermined because the sign of I_1 depends on the arbitrariness of ϕ by 60°.

[1] G. H. Wagnière, *On Chirality and the Universal Asymmetry: Reflections on Image and Mirror Image* (Wiley, Weinheim, 2008).
[2] L. D. Barron, Space Sci. Rev. **135**, 187 (2008).
[3] T. Kimura, Annu. Rev. Mater. Res. **37**, 387 (2007).
[4] S.-W. Cheong and M. Mostovoy, Nat. Mater. **6**, 13 (2007).
[5] S. B. Wilkins, P. D. Spencer, P. D. Hatton, S. P. Collins, M. D. Roper, D. Prabhakaran, and A. T. Boothroyd, Phys. Rev. Lett. **91**, 167205 (2003).
[6] U. Staub, V. Scagnoli, A. M. Mulders, K. Katsumata, Z. Honda, H. Grimmer, M. Horisberger, and J. M. Tonnerre, Phys. Rev. B **71**, 214421 (2005).
[7] F. Yakhou, V. Plakhty, H. Suzuki, S. Gavrilov, P. Burlet, L. Paolasini, C. Vettier, and S. Kunii, Phys. Lett. A **285**, 191 (2001).
[8] Y. Tanaka, K. Katsumata, S. Shimomura, and Y. Onuki, J. Phys. Soc. Jpn. **74**, 2201 (2005).
[9] D. H. Templeton and L. K. Templeton, Acta Crystallogr., Sect. A: Cryst. Phys., Diffr., Theor. Gen. Crystallogr. **36**, 237 (1980).
[10] D. H. Templeton and L. K. Templeton, Acta Crystallogr., Sect. A: Found. Crystallogr. **42**, 478 (1986).
[11] Y. Tanaka, T. Takeuchi, S. W. Lovesey, K. S. Knight, A. Chainani, Y. Takata, M. Oura, Y. Senba, H. Ohashi, and S. Shin, Phys. Rev. Lett. **100**, 145502 (2008).
[12] S. W. Lovesey, E. Balcar, and Y. Tanaka, J. Phys.: Condens. Matter **20**, 272201 (2008).
[13] Y. Tanaka, S. P. Collins, S. W. Lovesey, M. Matsumami, T. Moriwaki, and S. Shin, J. Phys.: Condens. Matter **22**, 122201 (2010).
[14] Y. Tanaka, T. Kojima, Y. Takata, A. Chainani, S. W. Lovesey, K. S. Knight, T. Takeuchi, M. Oura, Y. Senba, H. Ohashi, and S. Shin, Phys. Rev. B **81**, 144104 (2010).
[15] V. E. Dmitrienko, Acta Crystallogr., Sect. A: Found. Crystallogr. **39**, 29 (1983).
[16] T. Usui, Y. Tanaka, H. Nakajima, M. Taguchi, A. Chainani, M. Oura, S. Shin, N. Katayama, H. Sawa, Y. Wakabayashi, and T. Kimura, Nat. Mater. **13**, 611 (2014).
[17] J. M. Bijvoet, A. F. Peerdeman, and A. J. van Bommel, Nature (London) **168**, 271 (1951).
[18] J. Karle, Int. J. Quantum Chem. **18**, 357 (1980).
[19] W. A. Hendrickson, Science **254**, 51 (1991).
[20] D. Gibbs, D. E. Moncton, K. L. D'Amico, J. Bohr, and B. H. Grier, Phys. Rev. Lett. **55**, 234 (1985).
[21] Y. Hinatsu, Y. Doi, K. Ito, M. Wakeshima, and A. Alemi, J. Solid State Chem. **172**, 438 (2003).
[22] C. Ritter, A. Pankrats, I. Gudim, and A. Vorotynov, J. Phys.: Conf. Ser. **340**, 012065 (2012).
[23] E. A. Popova, N. Tristan, A. N. Vasiliev, V. L. Temerov, L. N. Bezmaternykh, N. Leps, B. Büchner, and R. Klingeler, Eur. Phys. J. B **62**, 123 (2008).
[24] Y. F. Popov, A. M. Kadomtseva, G. P. Vorob'ev, A. A. Mukhin, V. Y. Ivanov, A. M. Kuz'menko, A. S. Prokhorov, L. N. Bezmaternykh, and V. L. Temerov, JETP Lett. **89**, 345 (2009).
[25] M. Renninger, Zeitschrift für Kristallographie - Crystalline Materials **97**, 107 (1937).
[26] E. Weckert and K. Hümmer, Acta Crystallogr., Sect. A: Found. Crystallogr. **53**, 108 (1997).
[27] J. Kokubun, K. Ishida, D. Cabaret, F. Mauri, R. V. Vedrinskii, V. L. Kraizman, A. A. Novakovich, E. V. Krivitskii, and V. E. Dmitrienko, Phys. Rev. B **69**, 245103 (2004).
[28] S. W. Lovesey, E. Balcar, K. S. Knight, and J. Fernández-Rodríguez, Phys. Rep. **411**, 233 (2005).
[29] Y. Joly, Y. Tanaka, D. Cabaret, and S. P. Collins, Phys. Rev. B **89**, 224108 (2014).
[30] M. Takahashi (private communication).
[31] T. Stanislavchuk, E. Chukalina, M. Popova, L. Bezmaternykh, and I. Gudim, Phys. Lett. A **368**, 408 (2007).
[32] D. Volkov, A. Demidov, and N. Kolmakova, J. Exp. Theor. Phys. **106**, 723 (2008).
[33] A. V. Malakhovskii, A. L. Sukhachev, A. Y. Strokova, and I. A. Gudim, Phys. Rev. B **88**, 075103 (2013).
[34] K. Momma and F. Izumi, J. Appl. Crystallogr. **44**, 1272 (2011).